# Supporting Information

# Selective oxygen vacancy engineering for shrinking the potential barrier of S-scheme heterojunction toward highly efficient photocatalytic $CO_2$ conversion

**Yue Huang[a], Jinfeng Zhang[a], Olim Ruzimuradov[b,c], Shavkat Mamatkulov[b,c], Kai Dai[a,*], and Jingxiang Low[d,e,*]**

a. Key Laboratory of Green and Precise Synthetic Chemistry and Applications, Ministry of Education, Huaibei Normal University, Huaibei, Anhui 235000, P. R. China.
b. Turin Polytechnic University in Tashkent, Kichik khalqa yoli 17, Tashkent 100095, Uzbekistan.
c. Institute of Material Sciences, Uzbekistan Academy of Sciences, Chingiz Aytmatov 2b, 100084 Tashkent, Uzbekistan.
d. Hefei National Laboratory for Physical Sciences at the Microscale, University of Science and Technology of China, Hefei, Anhui 230026, P. R. China.
e. Multidisciplinary Platform of Advanced Engineering, Engineering, Chemical Engineering Discipline, School of Engineering, Monash University, Bandar Sunway 47500, Selangor, Malaysia.

## 1. Experimental Details

### Characterizations

The phase structure of the prepared samples was investigated by X-ray diffraction (XRD, Panalytical Empyrean diffractometer, Netherlands) measurements. UV-Vis diffuse reflectance spectroscopy (DRS) was recorded with a PerkinElmer Lambda 950. The morphologies of the composite samples were characterized by transmission electron microscopy (TEM, JEOL JEM-2010) and scanning electron microscopy (SEM, HITACHI Regulus 8220). Photoluminescence (PL) spectra were obtained through the FLS920 spectrometer. Fourier transform infrared spectroscopy (FT-IR) was tested on Nicolet iS50 spectrometer. The photoelectrochemistry of the prepared samples was measured by a Shanghai Chenhua CHI-660D workstation. For photoelectrochemical measurements, the electrolyte solution was 1 M $Na_2SO_4$. 20 mg catalyst, 50 μL 5% Nafion and 0.5 mL ethanol were evenly mixed, and then the sample was coated on ITO glass to prepare the working electrode. The Pt wire was used as the counter electrode, and the reference electrode was Ag/AgCl. The photocurrent curve was recorded by alternately turning on and off the light every 50 s. X-ray photoelectron spectroscopy (XPS) analysis

was performed on Thermo ESCALAB 250 spectrometer. In situ irradiated XPS (ISI-XPS) was performed by irradiating the characterization chamber using a 300 W xenon lamp as light source. The Barrett-Emmett-Teller (BET, ASAP 2060) method was used to calculate the specific surface area of the sample. Electron paramagnetic resonance (EPR) signals were collected on a Bruker EPR A300 spectrometer. In-situ Fourier transform infrared spectra was obtained over a DF-FTIR-100 Fourier transform infrared spectrometer. Atomic force microscopy was performed on Bruker Multimode 8 to study the thicknesses of the prepared sample. Raman spectroscopy was performed on a Raman spectrometer (HORIBA LabRAM HR Evolution).

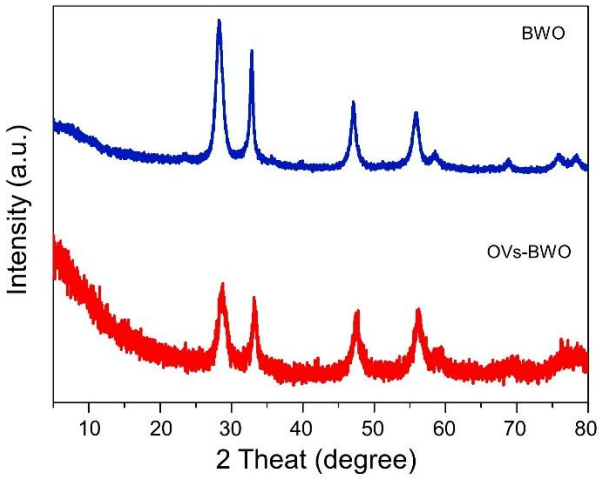


**Figure S1.** XRD patterns of BWO and OVs-BWO.

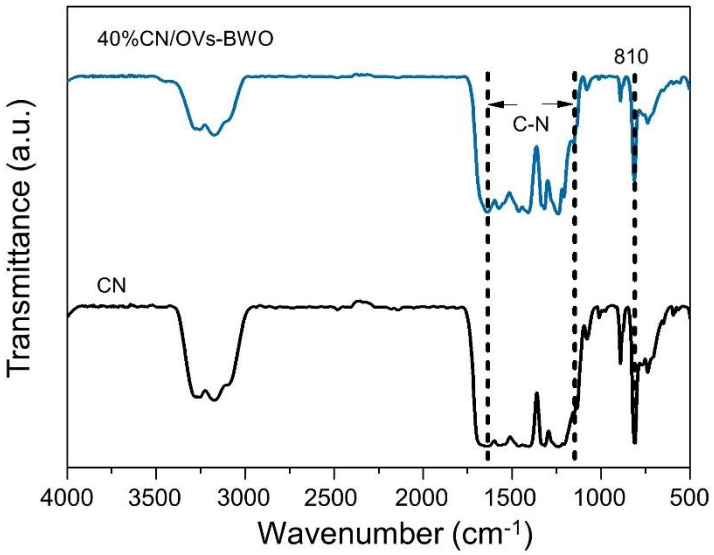


**Figure S2.** FT-IR spectra of CN and 40%CN/OVs-BWO.

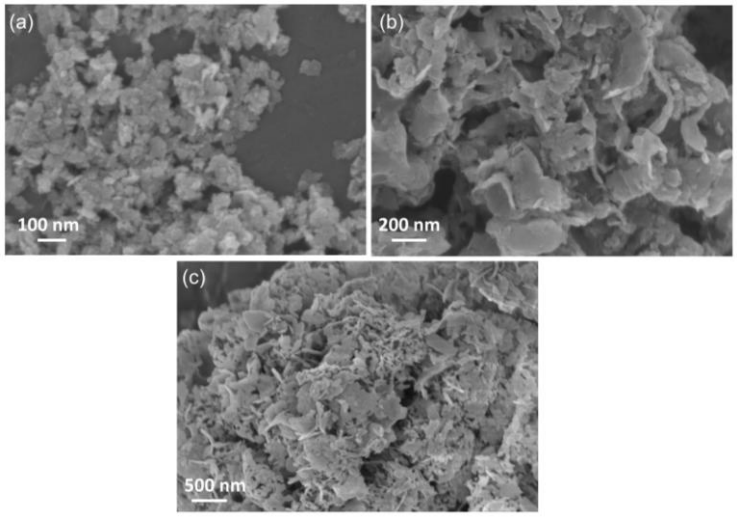


**Figure S3.** SEM images of (a) OVs-BWO, (b) CN and (c) 40%CN/OVs-BWO.

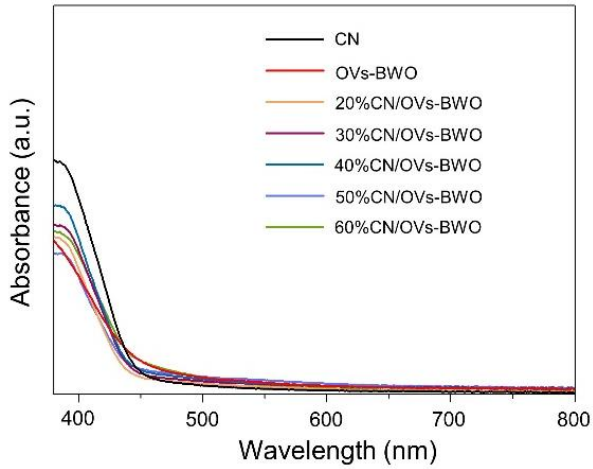


**Figure S4** Light absorption spectra of CN, OVs-BWO and CN/OVs-BWO loaded with different CN contents.

After coupling with the CN, the absorption band edges of the CN/OVs-BWO blue-shift with the increase in the CN contents.

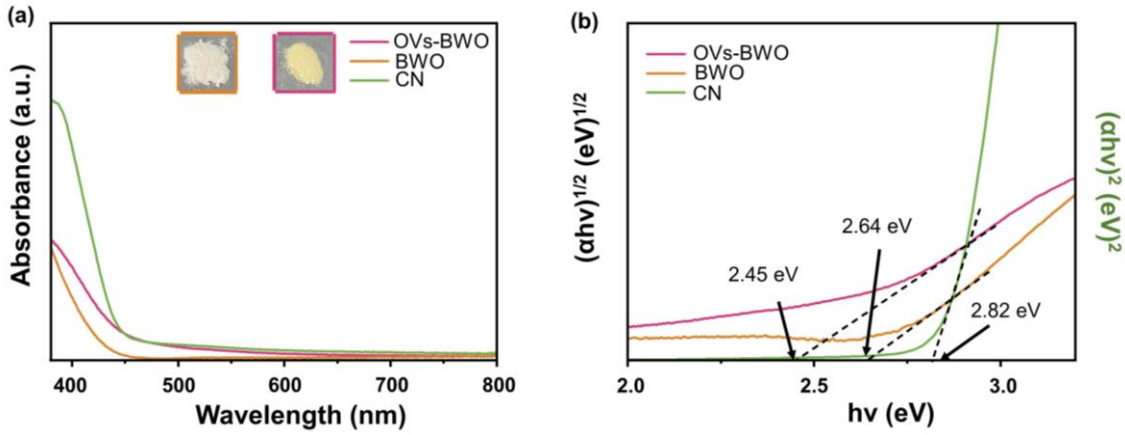


**Figure S5.** (a) Light absorption spectra of OVs-BWO, BWO and CN. (b) Plots of the $(\alpha h\nu)^{1/2}$ versus photon energy (hν) of OVs-BWO, BWO and CN($(\alpha h\nu)^2$).

As shown in Figure S5a, the absorption edge of BWO locates at around 438 nm, showing a light-yellow color. Upon introduction of the oxygen vacancies, the absorption edge of the OVs-BWO red-shifts to around 468 nm, further suggesting the presence of oxygen vacancies. The band gap can be obtained with the following equation[1,2]:

$$\alpha h\nu = A\left(h\nu - E_g\right)^{n/2}$$

$\alpha$ is the absorption coefficient, $h$ and $\nu$ are Planck's constant and light frequency, and $A$ is a constant. n is related to the type of semiconductor. Figure S5b shows that the OVs-BWO band gap is blue-shifted to 2.45 eV compared to BWO (2.64 eV), which can be attributed to the abundant defect states. CN band gap is 2.82 eV. The positive slopes of OVs-BWO and CN in the Mott-Schottky plots indicate that they are n-type. The flat-band potential was estimated from the x-intercept of the Mott-Schottky plot (Fig. S6). For n-type semiconductors, the conduction band minimum (CBM) is usually located slightly negative than the flat-band potential. Based on this approximation, the CB of OVs-BWO and CN at 1 kHZ are -0.42 and -1.29 V, respectively. The VB can be obtained by the following formula:

$$E_{VB} = E_g + E_{CB}$$

Thus, the VB of OVs-BWO is 2.03 V, and the VB of CN is 1.53 V.

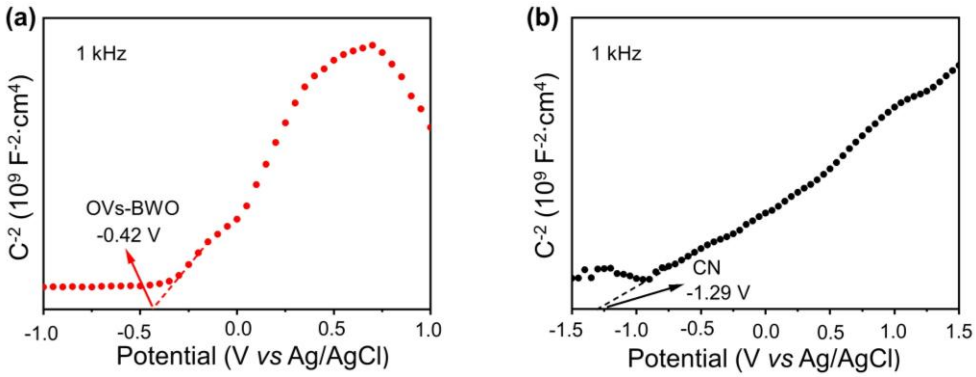


**Figure S6.** Mott-Schottky plots of (a) OVs-BWO and (b) CN measured at the frequency of 1 kHz.

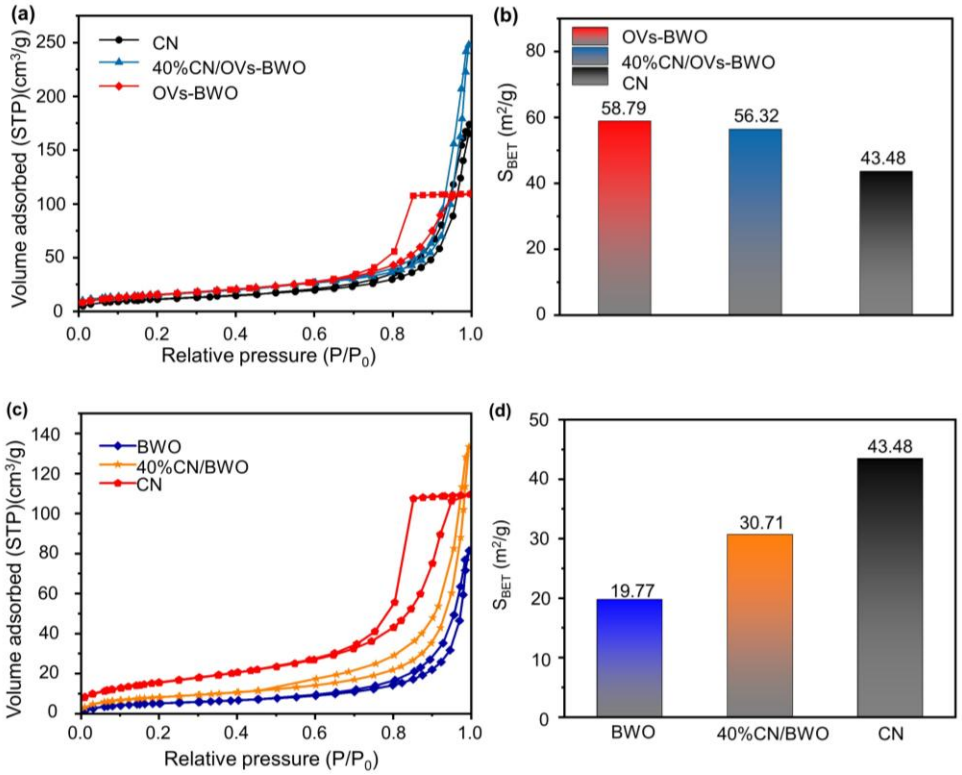


**Figure S7.** (a,b) $N_2$ adsorption-desorption isotherms (a) and (a) $S_{BET}$ of different prepared samples. (b) (c,d) $N_2$ adsorption-desorption isotherms curves (c) and $S_{BET}$ (d) of BWO, 40%CN/BWO and CN.

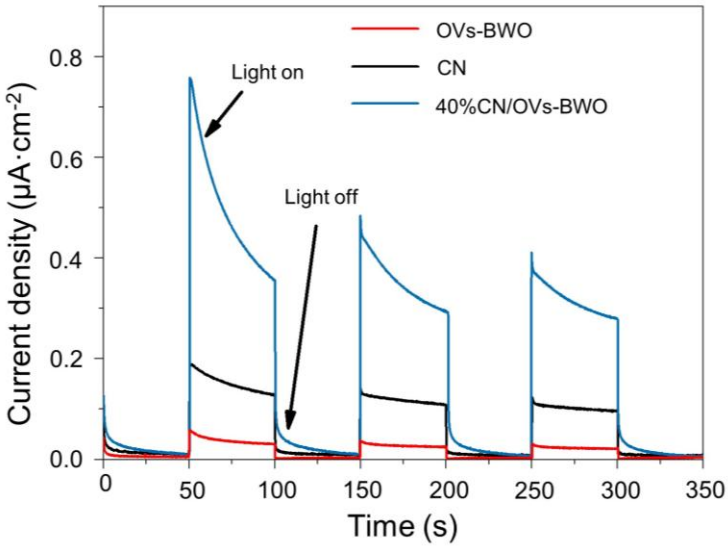


**Figure S8.** Transient photocurrent responses of CN, OVs-BWO and 40%CN/OVs-BWO.

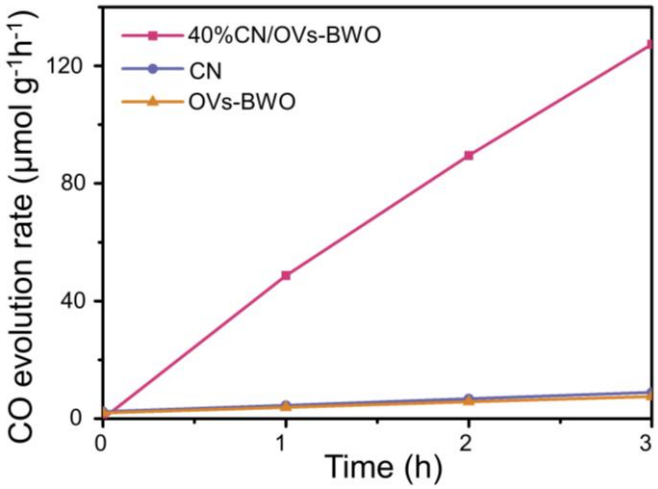


**Figure S9.** Time profile of CO production during photocatalytic $CO_2$ reduction.

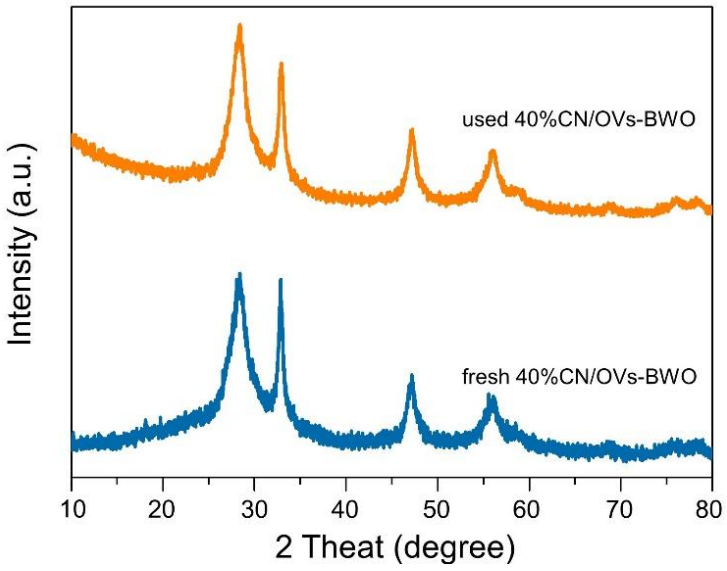


**Figure S10.** XRD patterns of 40%CN/OVs-BWO before and after the photocatalytic test.

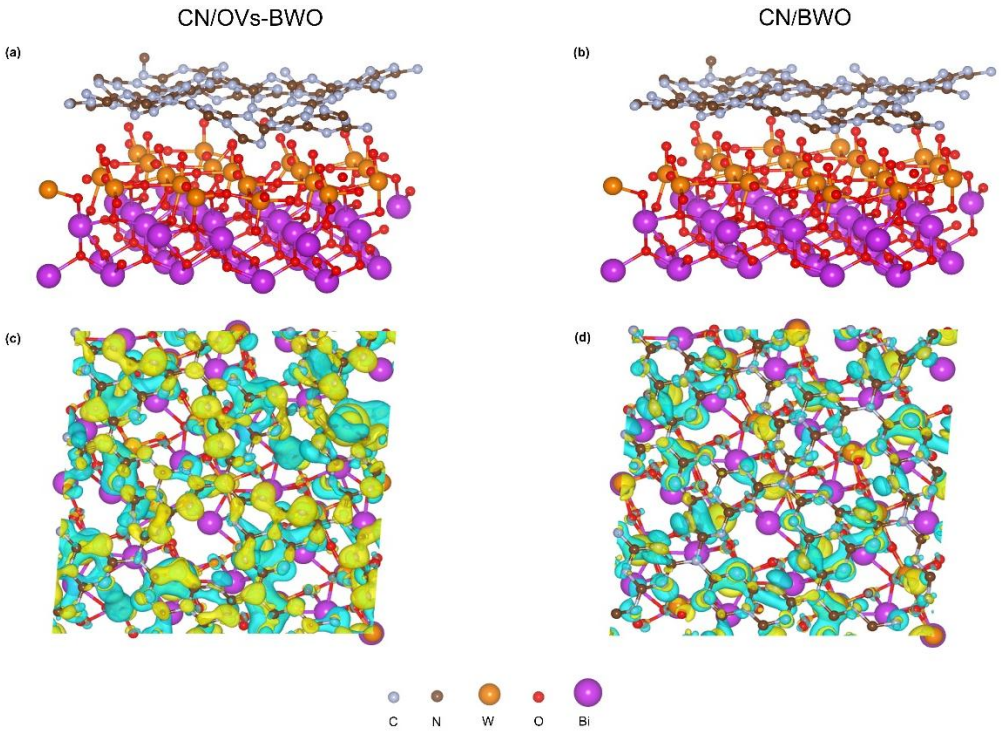


**Figure S11.** (a,b) Optimized structures of CN/OVs-BWO (a) and CN/BWO (b). (c,d) Top view of the charge density difference with an isosurface of $1*10^{-3}$ e/Å$^3$ of CN/OVs-BWO (c) and CN/BWO (d).

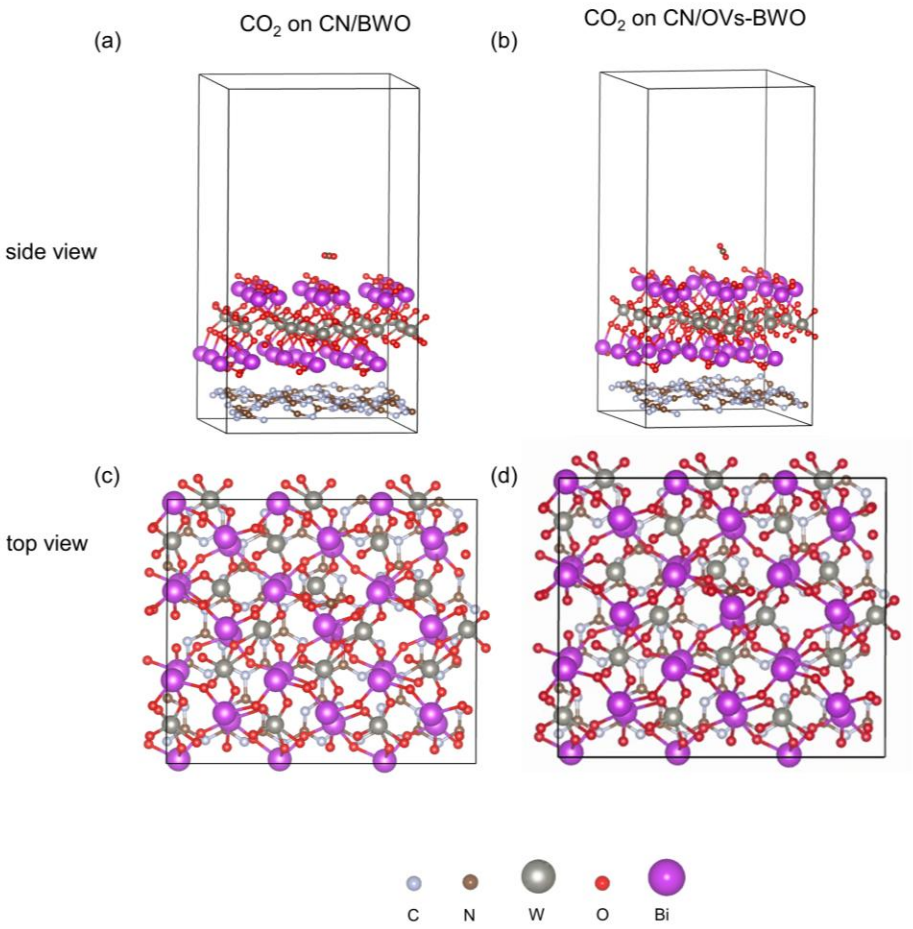


**Figure S12.** (a,b) Optimized structures of (a) $CO_2$ on CN/ BWO and (b) $CO_2$ on CN/OVs-BWO. (c,d) Top view of the charge density difference with an isosurface of $1*10^{-3}$ e/Å$^3$ of (c) $CO_2$ on CN/ BWO and (d) $CO_2$ on CN/OVs-BWO.

**Table S1.** Comparison of the photocatalytic $CO_2$ conversion of the 40%CN/OVs-BWO with the previously reported photocatalysts.

| **Sample** | **Light source** | **CO production rate ($\mu mol\ g^{-1}\ h^{-1}$)** | **References** |
|---|---|---|---|
| $RuO_2/Bi_2WO_6$ | 300 W Xe lamp | 0.9787 | [3] |
| $Cs_2AgBiBr6/Bi_2WO_6$ | 300 W Xe lamp | 48.5 | [4] |
| Ni-g-$C_3N_4$ (boron-oxo species) | 300W Xe lamp | 22.1 | [5] |
| $CNQDs/Bi_2WO_6$ | 300W Xe lamp | 26.24 | [6] |
| $1.5Fe\text{-}Bi_2WO_6$ | 300 W Osram light source | 36.78 | [7] |
| $2Ag\text{-}\ Bi_2WO_6$ | 300 W Xe lamp | 19.49 | [8] |
| HBWO@Br-COF-2 | 300 W Xe lamp | 19.9 | [9] |
| CN/OVs-BWO | 300 W Xe lamp | 48.65 | This work |

## References

[1] X. Li, J. Zhang, Y. Huo, K. Dai, S. Li, S. Chen. Two-dimensional sulfur- and chlorine-codoped g-$C_3N_4$/CdSe-amine heterostructures nanocomposite with effective interfacial charge transfer and mechanism insight. *Appl. Catal. B* 2021, 280, 119452. https://doi.org/10.1016/j.apcatb.2020.119452.

[2] S. Li, M. Cai, C. Wang, Y. Liu, N. Li, P. Zhang, X. Li. Rationally designed $Ta_3N_5$/BiOCl S-scheme heterojunction with oxygen vacancies for elimination of tetracycline antibiotic and Cr(VI): Performance, toxicity evaluation and mechanism insight. *J. Mater. Sci. Technol.* 2022, 123, 177-190. https://doi.org/10.1016/j.jmst.2022.02.012.

[3] H. Jiang, Q. An, S. Zang. Ultrathin $RuO_2$/$Bi_2WO_6$ and $PtO_2$-Pt/$Bi_2WO_6$ heterojunction nanosheets toward efficient photocatalytic $CO_2$ reduction under visible light irradiation. *J. Environ. Chem. Eng.* 2023, 11, 110960. https://doi.org/10.1016/j.jece.2023.110960.

[4] H. Wang, X. Wang, P. Hu, T. Liu, B. Weng, K.-h. Ye, Y. Luo, H. Ji. Vacancy pair induced surface chemistry reconstruction of $Cs_2AgBiBr_6$/$Bi_2WO_6$ heterojunction to enhance photocatalytic $CO_2$ reduction. *Applied Catalysis B: Environment and Energy* 2024, 351, 123956. https://doi.org/10.1016/j.apcatb.2024.123956.

[5] Y. Wang, Y. Qu, B. Qu, L. Bai, Y. Liu, Z.-D. Yang, W. Zhang, L. Jing, H. Fu. Construction of Six-Oxygen-Coordinated Single Ni Sites on g-$C_3N_4$ with Boron-Oxo Species for Photocatalytic Water-Activation-Induced $CO_2$ Reduction. *Adv. Mater.* 2021, 33, e2105482. https://doi.org/10.1002/adma.202105482.

[6] X. Zhang, L. Ai, C. Tan, M. Zha, Y. Li, N. Guo, D. Jia, L. Wang. Chemically bonded to construct S-scheme CNQDs/$Bi_2WO_6$ heterostructure: The Bi-N bonds as interfacial electronic channel boosting the efficient photocatalytic $CO_2$ reduction under simulated sunlight. *Sep. Purif. Technol.* 2025, 355, 129542. https://doi.org/10.1016/j.seppur.2024.129542.

[7] N.Q. Thang, A. Sabbah, C.-Y. Huang, N.H. Phuong, T.-Y. Lin, M.K. Hussien, H.-L. Wu, C.-I. Wu, N.N.T. Pham, P. Van Viet, C.-H. Lee, L.-C. Chen, K.-H. Chen. Tailoring atomically dispersed Fe-induced oxygen vacancies for highly

efficient gas-phase photocatalytic $CO_2$ reduction and NO removal with diminished noxious byproducts. *J. Mater. Chem. A* 2024, 12, 31847-31860. https://doi.org/10.1039/d4ta05778c.

[8] L. Zhao, H. Hou, L. Wang, C.R. Bowen, J. Wang, R. Yan, X. Zhan, H. Yang, M. Yang, W. Yang. Atomic-level surface modification of ultrathin $Bi_2WO_6$ nanosheets for boosting photocatalytic $CO_2$ reduction. *Chem. Eng. J.* 2024, 480, 148033. https://doi.org/10.1016/j.cej.2023.148033.

[9] Y. Wang, Z. Dai, J. Wang, D. Zhang, F. Zhou, J. Li, J. Huang. Scheme-II heterojunction of $Bi_2WO_6$@Br-COFs hybrid materials for $CO_2$ photocatalytic reduction. *Chem. Eng. J.* 2023, 471, 144559. https://doi.org/10.1016/j.cej.2023.144559.